Supporting Information for: "The influence of reef isostasy, dynamic topography, and glacial isostatic adjustment on the Last Interglacial sea-level record of Northeastern Australia"

Rovere, A.[1,2,*], Pico, T.[3,*],Richards, F.[4], O'Leary, M.,[5], Mitrovica, J.[6],

Goodwin, I.[7,8], Austermann, J.[9], Latychev, K.[6]

[1]Department of Environmental Sciences, Informatics and Statistics, Ca' Foscari University of Venice, IT

[2]MARUM., Center for Marine Environmental Sciences, University of Bremen,DE

[3]Earth & Planetary Sciences Department, UC Santa Cruz, Santa Cruz, USA

[4]Department of Earth Science & Engineering, Imperial College London, London, UK

[5]School of Earth Sciences, University of Western Australia Oceans Institute, Perth, AU

[6]Department of Earth and Planetary Sciences, Harvard University, Boston, USA

[7]Climalab, New South Wales, AU

[8]Climate Change Research Centre and Australian Centre for Excellence in Antarctic Science, University of New South Wales, AU

[9]Department of Earth and Environmental Sciences & Lamont-Doherty Earth Observatory, Columbia University, New York, USA

*A. Rovere and T. Pico contributed equally to this manuscript.

Constructing Earth models for mantle convection simulations.

Temperature Structure

Initial temperature fields are determined using a hybrid approach. In the upper mantle, seismic velocities are converted into temperature following the methodology of Richards et al. (2020), wherein a range of observational constraints on the covariation of V_S, temperature, attenuation and viscosity in Earth's upper mantle are used to invert for best-fitting parameters in an experimentally derived model of anelasticity at seismic frequencies (Yamauchi & Takei, 2016). The tomographic V_S model we use to obtain upper mantle temperature densities is SLNAAFSA, a version of the SL2013sv (A. J. Schaeffer & Lebedev, 2013) upper mantle model augmented with regional high-resolution tomographic studies in North America (SL2013NA; A. Schaeffer & Lebedev, 2014), Africa (AF2019; Celli, Lebedev, Schaeffer, Ravenna, & Gaina, 2020), and South America and the South Atlantic Ocean (SA2019; Celli, Lebedev, Schaeffer, & Gaina, 2020; see Hoggard et al., 2020 and Richards et al., 2023 for further details). Optimal anelasticity parameters determined for this model are: $\mu_0 = 75.9$ GPa; $\frac{\partial \mu}{\partial T} = -17.9$ MPa °C^{-1}; $\frac{\partial \mu}{\partial P} = 2.54$; $\eta_r = 10^{23.0}$ Pa s; $E_a = 489$ kJ mol^{-1}; $V_a = 0.63$ cm^3 mol^{-1}; and $\frac{\partial T_s}{\partial z} = 0.931$ °C km^{-1}. Note that to circumvent unrealistically high intralithospheric temperatures caused by crustal bleeding artefacts in the shallowest sections of the input tomography, we modify the thermal structure above the lithosphere-asthenosphere boundary (i.e., depth to the 1200°C isotherm) by assuming that temperature decreases linearly from this interface to the surface.

Below 400 km, temperatures are derived from thermodynamic modelling. Following Austermann et al. (2021), we assume a pyrolitic background mantle composition and use Perple_X alongside the thermodynamic database of Stixrude & Lithgow-Bertelloni (2011)

to generate a lookup table of anharmonic shear-wave velocities and densities, varying temperature from 300–4500 K in 50 K increments and pressure from 0–140 GPa in 0.1 GPa increments. At each depth, temperature-dependent discontinuities in density and seismic velocity caused by phase transitions are smoothed by adopting the median temperature derivative across a ±500°C swath either side of the geotherm (Schuberth & Bunge, 2009). Smoothed anharmonic velocities are then corrected for anelasticity using a Q profile determined using the approach of Matas & Bukowinski (2007), as outlined in Richards et al. (2023). Having smoothed and corrected the V_S lookup table, velocities from five different seismic tomographic models — LLNL-G3D-JPS (Simmons et al., 2015), S40RTS (Ritsema et al., 2011), SAVANI (Auer et al., 2014), SEMUCB-WM1 (French & Romanowicz, 2015), and TX2011 (Grand, 2002) — are converted into temperature, with values adjusted by a constant offset to ensure mean temperatures are consistent with the mantle geotherm (Schuberth & Bunge, 2009). Following Richards et al. (2023), we account for chemical heterogeneity in the lowermost sections of LLVPs, with the composition and thickness of these basal layers determined via geodynamic inversions of dynamic topography, geoid undulations and CMB excess ellipticity data sets (see Table S1 for details). In parts of the mantle where chemistry is not equivalent to a particular modelled endmember (pyrolite; mid-ocean ridge basalt, Workman & Hart, 2005; chondrite-enriched basalt, Tolstikhin & Hofmann, 2005; or iron-enriched pyrolite, Lee et al., 2010), properties appropriate for a mechanical mixture of the two components are calculated using the Voigt-Reuss-Hill approximation to average the elastic moduli. Within the chemically anomalous basal layers of the LLVPs, temperatures are determined separately for the two components and then

combined into a single array, with the boundary corresponding to the -0.65% V_S anomaly contour (Burke et al., 2008).

Note that, following Richards et al. (2023) and Davies et al. (2022), we high-pass filter the seismic velocity models within the 1000–2000 km depth range, in order to correct for vertical smearing of long-wavelength structure and obtain an acceptable fit to the observed long-wavelength geoid-to-topography ratio. This filtering is accomplished by multiplying the spherical harmonic coefficients, c_{lm}, of the seismic velocity fields with a monotonic truncation function, $f(l)$ that increases smoothly from 0 to 1 with spherical harmonic degree according to

$$f(l) = \begin{cases} -\left(\frac{l-l_{min}}{l_{max}-l_{min}}\right)^4 + 2\left(\frac{l-l_{min}}{l_{max}-l_{min}}\right)^2 & \text{for} l \leq l_{max} \\ 1 & \text{for} l > l_{max} \end{cases}$$

where $l_{min} = 1$ is the minimum spherical harmonic degree in the truncation at which $f(l) = 0$ and $l_{max} = 8$ is the maximum degree at which $f(l) = 1$. Between 300 km and 400 km depth, temperatures derived from the two parameterisations are smoothly merged by taking their weighted average.

Mapping Temperature to Density

To self-consistently convert these initial temperature fields into density distributions within ASPECT, we construct a radially averaged thermal expansivity profile that is compatible with both our upper and lower mantle V_S-to-density parameterisations. We also simplify our model calculations by assuming incompressible convection and therefore remove adiabatic increases in temperature and density with depth. Since heat flow measurements, xenolith geochemistry, seismic velocity, gravity, and topography observations suggest that compositional and thermal density contributions approximately balance each

other within the continental lithosphere (Jordan, 1978; Shapiro et al., 1999), we make these regions neutrally buoyant by resetting their temperature to the average of all external material at the relevant depth. Finally, chemical heterogeneity in the basal sections of LLVPs is modelled by setting layer thickness and compositional excess density equal to best-fitting values derived via geodynamic inversion (Richards et al., 2023; see Table S1 for adopted parameter values).

Our mapping from temperature to density can therefore be expressed using

$$\rho(z, T, C) = \rho_0 \left[1 - \alpha(z) \left(T' - T_0\right)\right] + \Delta\rho_C C \tag{1}$$

where $\Delta\rho_C$ represents compositional excess density, C is the compositional field index ($C = 1$ inside the LLVP basal layer; $C = 0$ elsewhere). $\rho_0 = 3330$ kg m^{-3} is the reference density, $\alpha(z)$ represents the radial thermal expansivity profile, $T_0 = 1600$ K is the reference temperature, and T' represents the temperature after subtraction of the adiabat ($T' = (T - T_{ad}) + T_0$). In total, this approach generates 15 separate density models comprising different combinations of tomographically inferred initial temperature distribution, dense basal layer thickness, and compositional density anomaly.

Viscosity Structure

Viscosity in each convection simulation is parameterised using three different radial profiles, $\eta_r(z)$ (S10, Steinberger et al., 2010; F10V1, Forte et al., 2010; F10V2, Forte et al., 2010), with lateral thermal variations in viscosity incorporated using

$$\eta(z, T) = \eta_0(z) \epsilon_C C \exp\left[-\epsilon_T(z) \left(T - T_0\right)\right], \tag{2}$$

where $\epsilon_T(z)$ is the thermal viscosity exponent ($\epsilon_T(z) = 0.01$ for 0 km $\geq z \geq$ 670 km; $\epsilon_T(z) = 0.005$ for 670 km $> z \geq$ 2891 km), $\eta_0(z)$ represents the prescribed radial viscosity

profile, and $\epsilon_C = 100$ represents the compositional viscosity exponent. The latter parameter applies to models in which the basal layers of LLVPs contain compositional anomalies ($C = 1$), since recent studies find that these regions likely contain smaller proportions of low-viscosity post-perovskite and larger volumes of high-viscosity silic phases (e.g., stishovite and seifertite) compared to background mantle material Richards et al. (2023). This inference is further supported by recent work demonstrating that geoid observations are better matched by model predictions when LLVP material is assigned a similar viscosity to its surroundings, indicating that thermal and compositional controls on viscosity may counterbalance one another in the lowermost mantle (Davies et al., 2022).

Numerical Model Parameterisation

Equipped with these temperature, density, and viscosity inputs, we predict the time-dependent evolution of mantle circulation forward from the present-day to 1.5 million years in the future. Since ASPECT does not include self-gravitation, we impose the radially varying gravity profile from Glišović & Forte (2015). Thermal conductivity is also varied as a function of depth using the values adopted in that study, while heat capacity is set to a constant value of 1250 J K^{-1} kg^{-1}. All simulations assume free-slip boundary conditions at both the surface and CMB. In the upper 1000 km of the mantle, our numerical grid has ∼30 km radial resolution, increasing to ∼ 90 km below this depth, while lateral resolutions in the same depth ranges are ∼80 km and ∼ 210 km, respectively. This resolution is achieved using an initial global mesh refinement of 4 and an adaptive refinement of 1 applied only to mesh points above 1000 km depth.

Calculating Relative Sea-Level Change Caused by Dynamic Topography

Using ASPECT, we calculate dynamic topography, h at each time step of our simulation from the predicted normal stress, σ_{rr}, applied to the surface using

$$h = \frac{\sigma_{rr}}{(\mathbf{g} \cdot \mathbf{n})\,\Delta\rho}, \tag{3}$$

where $(\mathbf{g} \cdot \mathbf{n})$ is the component of gravitational acceleration normal to the upper boundary and $\Delta\rho$ is the density difference between outer grid cells and the overlying material, assumed to be air in the ASPECT calculations (note that water loading in oceanic regions is accounted for in the post-processing steps described below). To circumvent the possible impact of transient numerical artefacts in early timesteps, we assume that the average rate of dynamic topography change between 0.5 and 1.5 Ma is the same as that experienced between the LIG and the present day and subtract this projected change from the predicted present-day field. We also account for the impact of plate motions over the intervening timespan, by translating the dynamic topography field calculated for the LIG into its present-day coordinates using the GPS-based plate velocity model of DeMets et al. (2010), before calculating the difference between this rotated prediction of LIG dynamic topography and its present-day equivalent. To directly compare predicted dynamic topography changes to LIG relative sea-level observations, we also account for changes in water loading caused by mantle dynamics. This correction adopts the framework described in Austermann & Mitrovica (2015) and incorporates our dynamic topography outputs alongside equivalent geoid predictions.

References

Auer, L., Boschi, L., Becker, T., Nissen-Meyer, T., & Giardini, D. (2014). Savani: A variable resolution whole-mantle model of anisotropic shear velocity variations based on multiple data sets. *Journal of Geophysical Research: Solid Earth*, *119*(4), 3006–3034.

Austermann, J., Hoggard, M. J., Latychev, K., Richards, F. D., & Mitrovica, J. X. (2021). The effect of lateral variations in earth structure on last interglacial sea level. *Geophysical Journal International*, *227*(3), 1938–1960.

Austermann, J., & Mitrovica, J. X. (2015). Calculating gravitationally self-consistent sea level changes driven by dynamic topography. *Geophysical Journal International*, *203*(3), 1909–1922.

Burke, K., Steinberger, B., Torsvik, T. H., & Smethurst, M. A. (2008). Plume generation zones at the margins of large low shear velocity provinces on the core–mantle boundary. *Earth and Planetary Science Letters*, *265*(1-2), 49–60.

Celli, N. L., Lebedev, S., Schaeffer, A. J., & Gaina, C. (2020). African cratonic lithosphere carved by mantle plumes. *Nature Communications*, *11*(92), 1–10. doi: 10.1038/s41467-019-13871-2

Celli, N. L., Lebedev, S., Schaeffer, A. J., Ravenna, M., & Gaina, C. (2020). The upper mantle beneath the South Atlantic Ocean, South America and Africa from waveform tomography with massive data sets. *Geophysical Journal International*, *221*, 178–204. doi: 10.1093/gji/ggz574

Davies, D. R., Ghelichkhan, S., Hoggard, M., Valentine, A., & Richards, F. D. (2022). Observations and models of dynamic topography: Current status and future directions. *EarthArXiv*, X55W5T.

DeMets, C., Gordon, R. G., & Argus, D. F. (2010). Geologically current plate motions.

Geophysical journal international, *181*(1), 1–80.

Forte, A. M., Quéré, S., Moucha, R., Simmons, N. A., Grand, S. P., Mitrovica, J. X., & Rowley, D. B. (2010). Joint seismic–geodynamic-mineral physical modelling of African geodynamics: A reconciliation of deep-mantle convection with surface geophysical constraints. *Earth and Planetary Science Letters*, *295*(3-4), 329–341.

French, S. W., & Romanowicz, B. (2015). Broad plumes rooted at the base of the Earth's mantle beneath major hotspots. *Nature*, *525*(7567), 95–99. doi: 10.1038/nature14876

Glišović, P., & Forte, A. M. (2015). Importance of initial buoyancy field on evolution of mantle thermal structure: Implications of surface boundary conditions. *Geoscience Frontiers*, *6*(1), 3–22.

Grand, S. P. (2002). Mantle shear–wave tomography and the fate of subducted slabs. *Philosophical Transactions of the Royal Society of London. Series A: Mathematical, Physical and Engineering Sciences*, *360*(1800), 2475–2491.

Hoggard, M. J., Czarnota, K., Richards, F. D., Huston, D. L., Jaques, A. L., & Ghelichkhan, S. (2020). Global distribution of sediment-hosted metals controlled by craton edge stability. *Nature Geoscience*, *13*, 504–510.

Jordan, T. H. (1978). Composition and development of the continental tectosphere. *Nature*, *274*(5671), 544–548.

Lee, C.-T. A., Luffi, P., Höink, T., Li, J., Dasgupta, R., & Hernlund, J. (2010). Upside-down differentiation and generation of a 'primordial' lower mantle. *Nature*, *463*(7283), 930–933.

Matas, J., & Bukowinski, M. S. (2007). On the anelastic contribution to the temperature dependence of lower mantle seismic velocities. *Earth and Planetary Science Letters*,

259(1-2), 51–65.

Richards, F. D., Hoggard, M. J., Ghelichkhan, S., Koelemeijer, P., & Lau, H. C. (2023). Geodynamic, geodetic, and seismic constraints favour deflated and dense-cored llvps. *Earth and Planetary Science Letters*, *602*, 117964.

Richards, F. D., Hoggard, M. J., White, N., & Ghelichkhan, S. (2020). Quantifying the relationship between short-wavelength dynamic topography and thermomechanical structure of the upper mantle using calibrated parameterization of anelasticity. *Journal of Geophysical Research: Solid Earth*, *125*, e2019JB019062. doi: 10.1029/2019JB019062

Ritsema, J., Deuss, A., Van Heijst, H. J., & Woodhouse, J. H. (2011). S40RTS: A degree-40 shear-velocity model for the mantle from new Rayleigh wave dispersion, teleseismic traveltime and normal-mode splitting function measurements. *Geophysical Journal International*, *184*, 1223–1236. doi: 10.1111/j.1365-246X.2010.04884.x

Schaeffer, A., & Lebedev, S. (2014). Imaging the north american continent using waveform inversion of global and usarray data. *Earth and Planetary Science Letters*, *402*, 26–41.

Schaeffer, A. J., & Lebedev, S. (2013). Global shear speed structure of the upper mantle and transition zone. *Geophysical Journal International*, *194*, 417–449. doi: 10.1093/gji/ggt095

Schuberth, B. S. A., & Bunge, H. P. (2009). Tomographic filtering of high-resolution mantle circulation models: Can seismic heterogeneity be explained by temperature alone? *Geochem. Geophys. Geosyst.*, *10*(5), Q05W03. doi: 10.1029/2009GC002401

Shapiro, S. S., Hager, B. H., & Jordan, T. H. (1999). The continental tectosphere and Earth's long-wavelength gravity field. *Lithos*, *48*(1-4), 135–152.

Simmons, N., Myers, S., Johannesson, G., Matzel, E., & Grand, S. (2015). Evidence for long-lived subduction of an ancient tectonic plate beneath the southern Indian Ocean. *Geophysical Research Letters*, *42*(21), 9270–9278.

Steinberger, B., Werner, S. C., & Torsvik, T. H. (2010). Deep versus shallow origin of gravity anomalies, topography and volcanism on Earth, Venus and Mars. *Icarus*, *207*(2), 564–577.

Stixrude, L., & Lithgow-Bertelloni, C. (2011). Thermodynamics of mantle minerals - II. Phase equilibria. *Geophysical Journal International*, *184*, 1180–1213. doi: 10.1111/j.1365-246X.2010.04890.x

Tolstikhin, I., & Hofmann, A. W. (2005). Early crust on top of the Earth's core. *Physics of the Earth and Planetary Interiors*, *148*(2-4), 109–130.

Workman, R. K., & Hart, S. R. (2005). Major and trace element composition of the depleted MORB mantle (DMM). *Earth and Planetary Science Letters*, *231*(1-2), 53–72.

Yamauchi, H., & Takei, Y. (2016). Polycrystal anelasticity at near-solidus temperatures. *Journal of Geophysical Research: Solid Earth*, *121*(11), 7790–7820.

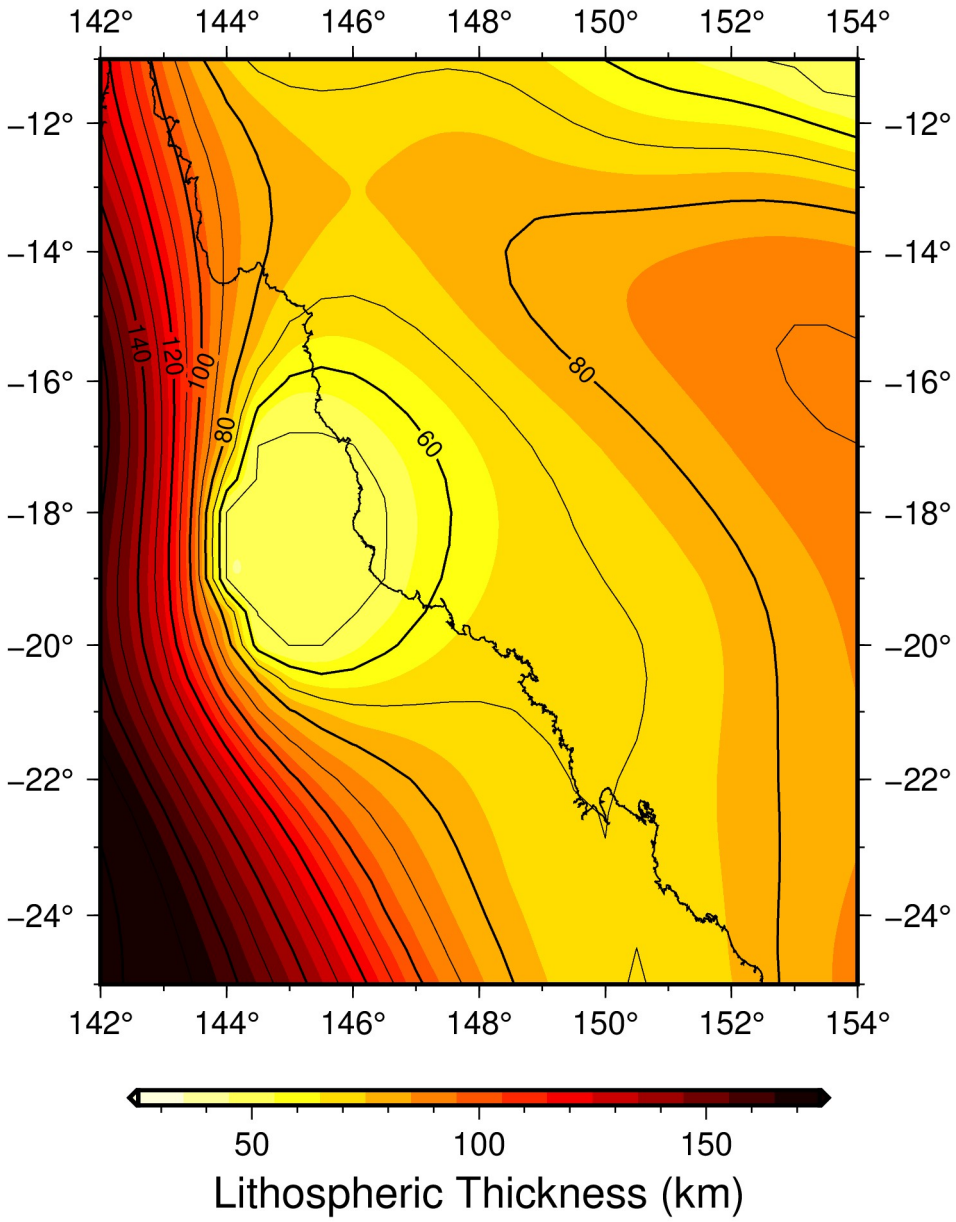

Figure S1. Lithospheric thickness variation in the Great Barrier Reef region. Note that lithospheric thickness is assumed to correspond to depth of 1175°C isotherm.

Table S1. Density characteristics of chemically anomalous material in basal LLVP layer. $\Delta\rho_C$ = intrinsic chemical density anomaly; MORB = present-day mid-ocean ridge basalt; CEB = chondrite-enriched basalt; FSP = iron-enriched pyrolite; bracketed percentages refer to percentage enrichment in a given compositional endmember with respect to pure pyrolite.

Tomographic Density Model	Viscosity Model	Compositional Endmember	Layer Thickness (km)	$\Delta\rho_C$
LLNL-G3D-JPS	S10	CEB (90%)	90	
LLNL-G3D-JPS	F10V1	FSP (100%)	90	
LLNL-G3D-JPS	F10V2	FSP (60%)	190	
TX2011	S10	CEB (53%)	200	
TX2011	F10V1	CEB (90%)	90	
TX2011	F10V2	MORB (92%)	190	
SEMUCB-WM1	S10	FSP (60%)	200	
SEMUCB-WM1	F10V1	FSP (60%)	190	
SEMUCB-WM1	F10V2	MORB (92%)	190	
SAVANI	S10	MORB (90%)	100	
SAVANI	F10V1	CEB (100%)	40	
SAVANI	F10V2	MORB (100%)	90	
S40RTS	S10	CEB (70%)	90	
S40RTS	F10V1	FSP (80%)	90	
S40RTS	F10V2	FSP (90%)	90	